EFDA–JET–PR(10)07

K.D. Lawson, K.M. Aggarwal, I.H. Coffey, F.P. Keenan, M.G. O'Mullane,
L. Ryć, J. Zacks and JET EFDA contributors

An Analysis of VUV C IV Emission from the JET Divertor Giving Measurements of Electron Temperatures

An Analysis of VUV C IV Emission from the JET Divertor Giving Measurements of Electron Temperatures

K.D. Lawson[1], K.M. Aggarwal[2], I.H. Coffey[2], F.P. Keenan[2], M.G. O'Mullane[3], L. Ryć[4], J. Zacks[1] and JET EFDA contributors*

JET-EFDA, Culham Science Centre, OX14 3DB, Abingdon, UK

[1]EURATOM-CCFE Fusion Association, Culham Science Centre, OX14 3DB, Abingdon, OXON, UK
[2]Astrophysics Research Centre, School of Mathematics and Physics, Queen's University, Belfast, BT7 1NN, Northern Ireland, UK
[3]Deptartment of Physics, University of Strathclyde, Glasgow, G4 0NG, UK
[4]Institute of Plasma Physics and Laser Microfusion, EURATOM Association, Hery 23 St, 01-497 Warsaw, Poland
** See annex of F. Romanelli et al, "Overview of JET Results", (Proc. 22 [nd] IAEA Fusion Energy Conference, Geneva, Switzerland (2008)).*

Preprint of Paper to be submitted for publication in
Plasma Physics and Controlled Fusion

ABSTRACT

A description of the radiation emitted by impurities from within a plasma is crucial if spectral line intensities are to be used in detailed studies, such as the analysis of impurity transport. The simplest and most direct check that can be made on measurements of line intensities is to analyse their ratios with other lines from the same ion. This avoids uncertainties in the plasma volume emitting the radiation and the absolute sensitivity calibration of the spectrometer and, in some cases, the need even for accurate measurements of parameters such as electron density. Consistency is required between the measured line intensity ratios and the theoretical values. For some elements, this can lead to the determination of parameters such as the electron temperature of the emitting plasma region.

Carbon was the main low Z intrinsic impurity in JET and an analysis of spectral line intensity ratios has been made for the C IV radiation emitted from the JET divertor. Agreement is found between the measured and theoretical ratios to within the experimental accuracy of ~ ±10%. This has allowed the electron temperature of the emitting region to be determined and estimates to be made of the contribution of charge exchange recombination to the electron energy level populations. The analysis has been made for a database of Ohmic and additionally heated phases of a large number of pulses and the importance of dielectronic and radiative recombination as well as ionization has been investigated. In addition, the development of T_e throughout two example discharges is illustrated.

The agreement found between the measured and theoretical C line intensity ratios for the C IV divertor emission contrasts with that from the JET scrape-off-layer, for which there are discrepancies.

1. INTRODUCTION

In order to use the passive emission from plasma impurities in detailed analyses, a description of the emitted radiation is required. This is provided by a collisional-radiative model, which enables the population of an excited state to be determined. When multiplied by the transition probability for spontaneous radiative decay, the intensity of the line emission due to the transition is obtained. The use of intensity ratios of lines emitted by the same ionization stage avoids the need to determine parameters such as the emitting plasma volume and the absolute sensitivity calibration of the spectrometer used for the measurements, thus increasing the reliability of the results.

If the theoretical model contains all relevant processes, there should be agreement between the measurements and the model to within the measurement accuracy. This is indeed found, for example, for a number of Na- and Li-like line intensity ratios, which were used to determine the short wavelength sensitivity calibration of the JET VUV SPRED survey spectrometer [5]. These lines are emitted from within the separatrix of the JET plasma. In contrast, emission from outside this boundary, from the Scrape-Off-Layer (SOL), did not give the expected consistency between theoretical and measured ratios. This paper analyses the C IV emission from a third region, the divertor plasma. C was the main low Z intrinsic impurity in the JET plasma, many of the plasma facing surfaces being manufactured from Carbon Fibre Composite (CFC) tiles. The analysis allows the electron temperature of the plasma region emitting the C IV radiation to be determined through a minimization procedure.

The divertor-viewing XUV/VUV spectrometer on JET, known locally as KT7, includes a double SPRED instrument. Its higher resolution detector, which is of particular value in that it has an independent relative sensitivity calibration, is ideal for studying the C IV spectrum as a number of unblended C IV lines fall within its spectral range. The spectrometer is described in section 2. Its sensitivity calibration is crucial in making accurate measurements of electron temperature and, hence, this is also discussed. The details of the collisional-radiative model are presented in section 3, while section 4 provides information on the minimization procedures. Section 5 presents the results, with section 5a those relating to a database of Ohmic, L-mode and H-mode measurements and section 5b to the time development of the electron temperature during two example pulses. Finally, our conclusions are given in section 6.

2. EXPERIMENTAL ARRANGEMENT

2.1. XUV/VUV SURVEY SPECTROMETER

The XUV/VUV spectrometer viewing the JET divertor [12] consists of three instruments, two SPRED spectrometers [4] and a Schwob-Fraenkel SOXMOS instrument [9]. It has a vertical line-of-sight looking from the top of the machine towards the JET divertor, as illustrated in figure 1. The diagnostic can be tilted poloidally allowing the line-of-sight to view anywhere from the inner divertor through to the SOL above the throat of the outer divertor. The Na- and Li-like line intensity ratios of intrinsic metals and gas-puffed Ar and Kr used to obtain the sensitivity calibration were recorded with this outermost line-of-sight and the C IV observations with a view into the divertor plasma. With the latter view, the radiation from the lower ionization stages of C is dominated by emission from the divertor. As can be seen in figure 1, the outermost view towards the SOL, still passes through the core plasma allowing the high temperature Li-like lines to be observed.

The SPREDs are enclosed in stainless steel shielding to reduce noise due to both neutrons and γ-rays, with 15cm of shielding between the plasma and detectors and 5cm thickness at the back and sides. The detectors are MicroChannel Plate (MCP) / phosphor combinations which are coupled to a Reticon photodiode array via a fibre optic bundle. It is the interaction of the neutrons and γ-rays with the MCP, with its high gain, that is of most concern. A shielding of 15cm of steel was expected to reduce the 2.5MeV neutron flux by a factor of ~8 and that of 8MeV γ-rays by a factor of ~17. Comparisons were made shortly after the double SPRED was first commissioned with the JET SPRED survey spectrometer, which is unshielded. These suggested that the background due to nuclear reaction products was a factor ~7 lower in the double SPRED than the unshielded instrument.

Originally, 0.5mm thick MCPs were installed in the double SPRED, but these were found to be very fragile. In 1998 they were replaced with MCPs that were 1mm thick, which also gave increased sensitivity. The MCPs have a CuI coating to enhance the electron emission. The double SPRED uses toroidal holographic gratings, that with the higher resolution having a ruling density of 2105g.mm^{-1}, the other with 450g.mm^{-1}. Both have extended and shifted spectral ranges compared to the standard SPREDs. The higher resolution instrument observes the wavelength range 140Å to

443Å with a spectral resolution of ~1Å. Normally the gratings used in the SPREDs enhance the first and third spectral orders; however, in the present case the second spectral order is weakly detected, but with a greater intensity than the third.

Both SPREDs have 2048 pixels, although the detector in the higher resolution instrument developed a fault in which adjacent pairs of pixels output the same reading, essentially reducing the useful number of pixels to 1024. A simple and reliable line integration method was employed, in which a fixed number of pixels on either side of the line centre define an integration range and the background to be subtracted. This method takes advantage of the similarity of the spectral line profile throughout the wavelength range of the instrument. The integration is performed using Simpson's rule. With 2048 pixels a ±5 pixel integration range is preferred. However, with only 1024 pixels a ±3 pixel range is ideal for intense lines, but is too wide for weak lines. For intense lines this range covers almost the full line profile, whereas a ±2 pixel range is assessed to be too narrow to ensure the most accurate integration for these lines. In the profile of weak lines, the third pixel on either side of the line centre tends to be absorbed into the background and therefore will not be reliable. Consequently, a ±2 pixel range is the maximum that can be used. The calibration is derived using intense lines for which the ±3 pixel range is appropriate. In order to measure weak lines the ratio of the ±3 to ±2 pixel integrations is also required, this being described by [6].

The design of the diagnostic is particularly robust making the spectrometer very stable mechanically. This is advantageous in running the instrument on JET with its long period of operations during which there is limited access to the machine.

2.2. SENSITIVITY CALIBRATION

An essential prerequisite to this study is the provision of a relative sensitivity calibration for the wavelength range of interest, its accuracy determining the stringency to which the model is tested and affecting that of the derived value of electron temperature. It was achieved for the higher resolution detector of the double SPRED by using a series of Na- and Li-like doublet line intensity ratios, which resulted in an exceptionally accurate relative calibration. The same method had previously been used for the short wavelength end of the JET SPRED survey spectrometer [5].

The Na- and Li-like doublets of a number of intrinsic metallic impurities are observed throughout the spectral range of the higher resolution double SPRED. They correspond to the $2p^6 3s\ ^2S_{1/2} - 2p^6 3p\ ^2P_{1/2,3/2}$ and $1s^2 2s\ ^2S_{1/2} - 1s^2 2p\ ^2P_{1/2,3/2}$ transitions, respectively. In addition, the noble gases Ar and Kr can be introduced into the plasma by gas puffing, these elements having a similar doublet structure. Figure 2 shows the spectrum for Pulse No: 67966, averaged between times 9.3 and 9.4s, with doublets belonging to Cr, Fe, Ni and Cu observed. In addition one of the Mn XXIII lines and the Ar XVI and Cr XIV doublets appear weakly in this spectrum. In contrast, the 192.0Å line of the Fe XXIV doublet is saturated and the Fe XXIII 132.9Å line, which is expected to be of similar intensity, can be seen weakly in the second and third orders. A comparison of the theoretical and measured doublet line intensity ratios yields the ratio of sensitivities at the doublet wavelengths.

Neighbouring doublets can then be used to extend the calibration to either shorter or longer wavelengths.

These intensity ratios are ideal for determining the sensitivity calibration, since they are found to be independent of n_e and are only very weakly dependent on T_e. They are modelled using a collisional-radiative model, which is described in section 3. Ratios were calculated at a temperature equal to the ionization potential and at half and double this temperature. Since the ratios differed by less than 2% over this wide temperature range, the values for the central temperatures were adopted. [8, 13] have provided relativistic distorted wave calculations of the electron collisional excitation rates for, respectively, the Na- and Li-like ionization stages for a wide range of elements. There are also R-matrix calculations for Ar XVI and Fe XXIV by [11]. Comparisons of the line intensity ratios modelled using the different electron rates, calculated with the ADAS atomic data package [10], show agreement to within ~1%. Interpolated values were obtained for those elements for which there are no published data and an adjustment was made to account for the marginally higher (~1%) Ar XVI and Fe XXIV R-matrix values. It is expected that the derived line intensity ratios are accurate to a few percent. In all, ten doublet ratios were used, their wavelengths extending from 153.5Å up to 412.0Å, almost the complete range of the higher resolution detector.

The detailed analysis of the Na- and Li-like doublets, described by [6], suggests a particularly good accuracy for the calibration more typical of the visible spectral region rather than of the VUV. Nevertheless, given the step-by-step procedure for its derivation, it is important to have confirmation of the calibration to ensure that there is no cumulative error. This can be provided by the C IV line intensity ratios emitted from the divertor plasma. Again, theoretical and measured line intensity ratios are compared. However, in this case, the model is more complicated, since the C IV ratios depend on electron temperature and recombination (particularly charge exchange recombination) must be considered as a populating mechanism. This is discussed further in section 3. Six C IV lines were used in the analysis. They are listed in table 1 and can be seen in figure 3, which shows the spectrum of Pulse No: 69931 recorded between times 2.3 and 2.6s. A check was made as to the effect of the C III line at 386.2Å on the integration of the 384.1Å line; this was found to be at most 2%. The three lowest wavelength lines are comparatively weak, a ±2 pixel range being used for their integration. Ratios were measured during the Ohmic phase in 86 pulses and the additionally heated phase in 165 pulses. In applying the model, the differences between the measured and theoretical ratios were minimized. Further information about this procedure is given in section 4.

It was clear from the analysis that overall the C IV line intensity ratios were consistent with the derived calibration. Differences for the individual line intensity ratios averaged over both databases are less than 9%. An exception was the 384.1Å / 312.4Å ratio, which had a difference of 16.5%, although this was in part due to the deviation of the Ar XVI 389.1Å point by ~7% from the general trend of the calibration. Given this consistency, the most accurate calibration will be obtained by combining the Na- and Li-like results with those of C IV, supposing that differences in the C IV line ratios are due to discrepancies in the calibration. A second order polynomial fit was made to both sets

of data. Since the measured C IV ratios depend on the calibration it was necessary to repeat the fits, two iterations being required before subsequent changes in the calibration were less than 1%. Inclusion of the C IV data led to changes in the calibration of at most 13%, at a wavelength of 419.6Å, -5% at 384.1Å and less than 2% at shorter wavelengths. The relative sensitivity calibration and final polynomial fit are shown in figure 4, the sensitivity being normalized to that at 312.4Å. This whole procedure is justified in that the resulting polynomial fit is close to a straight line in logarithmic space, falling between the Ar XVI 389.1Å and C IV 384.1Å points. The resulting calibration is expected to be accurate to ±10% throughout the wavelength range that includes the C IV lines.

3. THE COLLISIONAL-RADIATIVE MODEL

The calculation of the spectral line intensity of a transition from state i to j,

$$I_{ij} = n_i A_{ij} \quad \text{photons.s}^{-1},$$

requires knowledge of both the Einstein spontaneous emission transition probability, A_{ij}, and of the excited level population, n_i. In the collisional-radiative model, n_i is determined from the rate equations in which level *i* is populated both by collisional excitation and de-excitation and by radiative decay, the positive terms in equation (1), these same processes also resulting in depopulation of level i, which gives rise to the negative terms in the equation,

$$\frac{dn_i}{dt} = n_e \sum_{j \neq i} n_j q_{ji} - n_e \sum_{j \neq i} n_i q_{ij} + \sum_{j>i} n_j A_{ji} - \sum_{j<i} n_i A_{ij} + \alpha. \qquad (1)$$

q_{ij} is the collisional excitation or de-excitation rate from level i to j and the final term α denotes contributions from recombination processes. The electron collisional ionization from the C IV excited levels was checked using the semi-classical Exchange Classical-Impact Parameter (ECIP) approximation [2] contained in the ADAS package and was found to be negligible. Ionization from C III is expected to terminate mainly in the C IV ground level and therefore will not affect the balance of the populations in the excited levels. There has been no indication in the analysis that this process is significant and so has been omitted from equation (1). In contrast, the final state of the ion after recombination, whether dielectronic, radiative, three-body or charge-exchange, is likely to be an excited level, with the population of that level being increased. In the steady state approximation,

$$\frac{dn_i}{dt} = 0,$$

this leading to a set of simultaneous equations, which can be solved for n_i / n_g, where n_g is the ground level population. Hence, in addition to the transition probabilities, collisional excitation and de-excitation rates are required, as well as various recombination coefficients. For ions such as C IV, the main populating mechanism is electron collisions and [1] have provided new transition

probabilities and R-matrix calculations of the electron collision strengths for this ion, the latter for a wide range of energies. The recombination coefficients were compiled from various sources by [7] and are available in the ADAS database.

A convenient form of the collisional-radiative model is provided within the ADAS package by the Photon Emissivity Coefficient (PEC) formulation. In this treatment, the summation terms in equation (1) are combined into a single coefficient relating to electron collisional excitation and radiative decay called the excitation PEC, ε^{exc}. This coefficient is a function of T_e and n_e. Corresponding PECs can be derived to give free electron recombination, ε^{rec}, and charge exchange recombination, ε^{cx}, contributions to the level populations, so that the line intensity becomes

$$I = n_e\, n_g \varepsilon^{exc} + n_e n_{g+1} \varepsilon^{rec} + n_D n_{g+1} \varepsilon^{cx},$$

where n_{g+1} is the ground level population of the next higher ionization stage and n_D the neutral D density, this ion giving rise to the most significant charge exchange contribution. The free electron recombination PEC includes contributions representing dielectronic, radiative and three body recombination, although only the first two are expected to be significant at the densities of interest. Line intensity ratios can be expressed as

$$\frac{I_1}{I_2} = \frac{\varepsilon_1^{exc} + \dfrac{n_{g+1}}{n_g}\varepsilon_1^{rec} + \dfrac{n_D n_{g+1}}{n_e n_g}\varepsilon_1^{cx}}{\varepsilon_2^{exc} + \dfrac{n_{g+1}}{n_g}\varepsilon_2^{rec} + \dfrac{n_D n_{g+1}}{n_e n_g}\varepsilon_2^{cx}}.$$

4. THE MINIMIZATION ROUTINES

In order to test the model and thereby determine the electron temperature, fractional differences between the measured and theoretical line intensity ratios are found and the RMS difference minimized. This was achieved by varying T_e, $\log_{10}n_e$, n_{g+1}/n_g and $n_D n_{g+1}/n_e n_g$. It was found that for the pulses studied in this paper the minimization was not sensitive to n_e or the ratio n_{g+1}/n_g, the latter forming part of the free electron recombination term. However, a value of n_e was still required in the model and this was arbitrarily fixed at $10^{18}m^{-3}$. Subsequently, only T_e and the ratio of densities from the charge exchange term, $n_D n_{g+1}/n_e n_g$, were varied.

Two minimization routines were used. The first checked a matrix of discrete points in either the 4 or 2 variable space, while the second used the 'Constrained_Min' IDL procedure. In the second the variables were constrained to the ranges given in table 2. The range in T_e extends from just above the temperature of maximum ion abundance of C IV under ionization equilibrium (~7.5eV) to double its ionization potential (64.5eV). That of n_e encompasses densities at which the low density limit approximation can be applied to C IV up to the highest that might be expected in the JET divertor. In the case of the density ratios, ranges were chosen that allowed recombination to be

either negligible or a dominating populating mechanism. Differences in T_e determined by the two methods were generally less than a few per cent, the average difference, for example, for the Ohmic database being less than 2%.

The six C IV lines listed in table 1 were used in the analysis, these normally being unblended. Ratios between all lines were considered, differences in the derived value of T_e of up to 20% being found. The ratios with the 312.4Å line were found to give near median values of T_e and, since this transition is intense, always detected and rarely blended, ratios with this line were used in the present analysis. Checks were made to investigate the effect of excluding one ratio from the minimization. It was clear that the omission of the ratio including the 419.6Å line seriously affected the determination of T_e and the 312.4Å line was essential to fix the magnitude of the charge exchange component. This is understood in that the charge exchange contribution is largest for this line. Both of these lines are intense and usually unblended so their inclusion in the minimization does not limit the analysis. Removal of a ratio involving one of the other lines from the analysis led to differences in T_e of, on average, ≤10%.

Other factors that affect the accuracy of the measured value of T_e are the relative sensitivity calibration of the spectrometer and the accuracy of the atomic data used. The sensitivity calibration has been discussed in section 2b, its accuracy being ±10% in the region in which the C IV lines are observed. As noted in section 3, new atomic data has been generated for this analysis [1]; the energy levels and radiative rates are expected to be accurate to better than 1% and 10%, respectively, the collision strengths from which the rates are derived to 20% in general, but better than 10% for the transitions considered here. This is consistent with the differences found between the measured and theoretical ratios. The RMS difference for each measurement averaged over the individual databases varied between 2 and 10%. This range includes minimizations made using the matrix method and the 'Constrained_Min' IDL procedure. It also includes cases in which both the calibration that has been derived from only the Na- and Li-like ratios and the preferred one modified by the C IV data have been used, as well as examples when ratios with different C IV lines were tested and when one ratio was excluded from the minimizations.

The importance of the collisional rates on the accuracy can be illustrated in the case in which the charge exchange contribution is small. Even at densities of ~10^{19} m^{-3}, the C IV system is close to its low density limit, in which nearly all the population is in the ground level. The population of the $1s^2 2p$ levels is $<2\times10^{-3} n_g$ and higher levels $<10^{-6} n_g$. In this limit, the dominant mechanisms in determining the excited level populations are electron collisional excitation from the ground level with a smaller contribution from charge exchange recombination, balanced by radiative decay. Neglecting charge exchange, the excited level population is

$$n_i \approx \frac{n_e n_g q_{gi}}{\sum_{j<i} A_{ij}} ,$$

resulting in line intensity ratios of

$$\frac{I_{ij1}}{I_{kl1}} \approx \frac{q_{gi} A_{ij1}}{q_{gk} A_{kl1}} \frac{\sum_{l<k} A_{kl}}{\sum_{j<i} A_{ij}} .$$

It can be seen that, for line ratios in which a single transition dominates the radiative decay of each line, the transition probabilities cancel, so that

$$\frac{I_{ij}}{I_{kl}} \approx \frac{q_{gi}}{q_{gk}},$$

the line intensity ratio approximating to the ratio of the electron collisional rates from the ground level to the levels of interest. In the present study, this applies particularly to the n = 2−3 transitions and to a lesser extent to the n = 2−4 transitions. For these cases, the accuracy of the collisional rates is crucial in determining that of the theoretical line intensity ratios.

Given the above accuracies, a realistic estimate of the uncertainty of the T_e measurement is expected to be ±20%, this being an upper limit on the typical variations found for T_e. We note that the observed spread in the data in the parameter dependences illustrated in section 5 is generally within this figure. It is also of interest to check the differences when an older C IV dataset compiled by [3] is used. This results on average in a 19% difference in the T_e measurement. It is noted that Burke used non-relativistic R-matrix calculations in the LS coupling scheme, which contrasts with those of [1] for which the fully relativistic GRASP code has been used. In addition, [1] included the n=5 levels in their calculations, which were performed for a much wider energy range giving effective collision strengths up to a temperature of 130eV as compared with Burke's 31eV. Burke's calculated data therefore required extrapolations to be made up to the appropriate high temperature limits. Further improvements in the electron collisional excitation rates are expected to result in much smaller differences.

The accuracy of the charge exchange contribution to the level populations is expected to be somewhat poorer than that for T_e and is estimated to be ~30-40%. This is because the charge exchange term in the minimization is always smaller than the excitation term, the latter being most important in determining T_e. For the charge exchange contributions, the crucial aspect is the relative accuracy of the 384.1Å and 312.4Å charge exchange recombination coefficients.

The *Constrained_Min* IDL routine was used to obtain all the results discussed in the next section.

5. RESULTS

5.1. DATABASE OF OHMIC, L-MODE AND H-MODE PULSES

A study was made of a database containing measurements of 86 Ohmic, 70 L-mode and 95 H-mode plasmas, of which 59 corresponded to ELMy H-mode and 36 to ELM-free H-mode phases. All the pulses used D as fuel. The C IV line intensity ratios were derived by averaging over as large an interval as possible, this varying from 0.3s to nearly 8s. No particular selection of pulses was made, with all pulses from the first observation of the divertor plasma since the diagnostic was

recommissioned in 2006 being considered in order to make the results as general as possible. The only pulses excluded were those in which there was strong impurity gas-puffing. There were relatively few pulses during the period of operations from which the pulses were taken with strong Ne or Ar gas-puffing, although a significant number contained He. The KT7/2 spectrum itself was used to ensure that only pulses with very low levels of He formed the database.

As already indicated agreement is found for all sections of the database between the measured and theoretical line intensity ratios to within the experimental errors, ~±10%. The implication is that the description of the impurity line intensities used is complete. This good agreement led to the C IV database being used in an iterative procedure to modify the independent Na- and Li-like spectrometer sensitivity calibration. The final calibration derived using both the Na- and Li-like line intensity ratios and the C IV ratios is preferred, since the deviation of the Ar XVI 389.1Å point from the general trend of the original calibration was unexpected and the final calibration derived is very close to a straight line in logarithmic space (figure 4). The results presented in this section therefore use this preferred calibration. Nevertheless it is appropriate to consider the effect of this modification to the calibration on the derived value of T_e. The change to the calibration due to the use of the C IV data is small, at most 13%, leading to (on average) a 14% difference in the value of T_e. The results for T_e using the entirely independent Na- and Li-like calibration are typically 14% lower, which are within the estimated uncertainties in the T_e measurement.

Solving the time dependent rate equation (1), shows that the 1/e times required to reach equilibrium and hence satisfy the steady state assumption are close to the reciprocal of the transition probabilities of the radiative decay, ~10^{-9} to 10^{-11}s. Again this is consistent with the system being close to the low density limit, in which the excited levels can be treated independently. It follows that the line intensity ratios will reflect the local conditions of temperature and density, adapting very rapidly and on a much shorter timescale than those of plasma processes to changes in these parameters.

In figure 5, the charge exchange densities ratio, $n_D n_{g+1}/n_e n_g$, is plotted against the electron temperature of the C IV emitting plasma region in the JET divertor, subsequently denoted T_e(C IV). It can be seen that most of the points fall in a triangular region with a clear upper boundary, limiting high temperature points to a low densities ratio. There are two groups of exceptional measurements, a series of Ohmic points whose measurement time began early in the discharge, before 2.5s, and some high lying L-mode and ELMy H-mode measurements. The latter are from a period of operations when there was Ne puffing and, although Ne was not used at the time of the measurement, it is thought that there was some contamination. Measurements made when Ne is being puffed lie in the same area of the diagram as these points.

Excluding these exceptional cases, the percentage charge exchange contributions to the 312.4Å and 384.1Å lines can also be plotted against T_e(C IV), shown in figures 6 and 7, respectively. These are the only significant charge exchange contributions for this ionization stage. In the case of the 312.4Å contribution, the excitation and charge exchange PECs have similar temperature dependences, resulting in a close correspondence between the charge exchange contribution and

the charge exchange densities ratio (figure 5). In contrast, the charge exchange PEC for the 384.1Å line decreases marginally with increasing temperature, while a clear increase is seen for the excitation PEC. Hence, the percentage charge exchange contribution to the 384.1Å line decreases markedly with temperature, as can be seen in figure 7. None of the PECs used that are large enough to affect the analysis have a dependence on electron density at the low densities of interest and therefore the minimization is not found to be sensitive to the density of the emitting region. Similarly, the minimization is not sensitive to the density ratio n_{g+1}/n_e for the pulses used in the present study. It follows that the recombination terms included in the free electron recombination PEC, those for dielectronic and radiative recombination being the most significant, must nevertheless be small, with any contribution being less than a few per cent.

It is instructive to separate the measurements of figure 5 into two groups, one containing Ohmic and L-mode and the other H-mode measurements. These are shown without the exceptional pulses described above in figures 8a and 8b, respectively. The figures illustrate the much wider range of C IV Ohmic and L-mode temperatures than is found for the H-mode cases. This may be due to the steeper edge gradients occurring in the H-mode plasmas leading to a more restricted range of transport parameters, a topic of interest for further study. The same feature can be seen in figure 9 which shows T_e(C IV) as a function of the volume averaged electron temperature of the bulk plasma. The H-mode points fall into a narrow band (figure 9b), whereas the Ohmic and L-mode measurements (figure 9a) occupy a much wider space, in which trends for each regime can be discerned. There is scatter in the data, the dotted lines in these diagrams acting as a guide to the trends.

Figure 10 shows the dependence of the temperature of the divertor C IV emitting region on the electron density of the bulk plasma. In figure 10a, all the Ohmic measurements, including those starting before 2.5s, are shown plotted against a line-integrated n_e. The measurement is made using an interferometer, which has a vertical line of sight cutting the bulk plasma close to its outer edge. In figures 10b and 10c the volume averaged n_e of the bulk plasma measured by LIDAR is used. Figure 10b includes the L-mode cases in addition to the Ohmic data, which can be seen to have a similar dependence to that seen in figure 10a. The L-mode points separate into two bands, one of which overlays the Ohmic data. All but three of these data points have low D_α emission (<9.0 $ph.s^{-1}.m^{-2}.sr^{-1}$) as measured at the outer divertor target. As in figure 9b, the H-mode data again forms a narrow band of points (figure 10c).

5.2. TIME HISTORIES OF ELECTRON TEMPERATURE

We have considered the time development of the electron temperature of the C IV emitting region of the divertor plasma, T_e(C IV), in two pulses. The first, Pulse No: 69937, is a D fuelled, H minority, 2.6T, 2.5MA H-mode discharge. It has both Neutral Beam Injection (NBI) and Ion Cyclotron Resonance Heating (ICRH). Their waveforms and the volume averaged T_e and n_e determined from the LIDAR diagnostic are shown in figure 11, together with the C IV divertor 312.4Å and 289.2Å line intensities and the D_α signal measured along an outer vertical line-of-sight. The pulse has

ELM-free periods leading up to three giant ELMs and the H-mode appears to be briefly lost after each giant ELM. However, the discharge quickly returns to a period of ELMy H-modes which in turn lead into the next ELM-free period or to an L-mode phase as the additional heating is stepped down towards the end of the pulse. Figure 12 shows the time development of T_e(C IV), together with the timing and relative magnitude of the larger ELMs. It is clear that the giant ELMs lead to a significant rise in the divertor T_e(C IV), there being a fall in the volume averaged T_e of the bulk plasma. The D charge exchange contributions to the 312.4Å and 384.1Å lines are shown in figure 13 and are typically ~20% and 2%, respectively, throughout the period of interest. Nevertheless, it is noted that drops in the contributions are observed immediately after the giant ELMs, particularly after the second and third.

In contrast to the database, where the electron temperature for each measurement represents an average over a period of time, the time history gives a measurement for each scan of the spectrometer. Nevertheless, it was necessary to smooth the time histories of the C IV line intensities prior to the minimization procedure in order to reduce the significant scatter in the data.

The second example, Pulse No: 69957, is of an advanced tokamak scenario discharge in which an Internal Transport Barrier (ITB) develops. This D fuelled discharge, with a H minority gas, uses a high toroidal field of 3.4T. The plasma current is ramped from ~1 to 2.7MA throughout the period of interest. There is NBI, ICRH and Lower Hybrid Current Drive (LHCD) as well as Ni laser ablation and a small amount of gas puffing of an Ar / Ne mixture. In addition to the heating waveforms, figure 14 shows the LIDAR volume averaged T_e and n_e and an ECE measurement of T_e towards the plasma edge, the C IV divertor 312.4Å, 289.2Å and 244.9Å emission and the vertical D_α intensity. Much of the data for the edge measurements of T_e recorded using ECE were noisy and, although not the outermost, the temperature at a major radius of 3.82m was chosen as this is relatively free of noise. Its shape is similar to the time histories of T_e at other close radii. The C IV 289.2Å and 244.9Å line intensities have been increased in the diagram by factors of 4 and 6 respectively. In figure 15, T_e(C IV) is shown, together with the additional heating and gas puffing waveforms to allow an easy comparison of the timings. In the case of the D and H, the trace shows the total rate at which the gases are released into the plasma edge. For the Ar / Ne mixture, this rate is rather different from the time history of the emission and hence cooling. Instead, the time development of the emission itself is illustrated in the diagram.

In this pulse the analysis proved to be difficult between 4.5 and 6.3s. The C IV line emission is relatively weak during this period and there are higher levels of Ni present than at other times. All three of the weaker C IV transitions were affected to some extent, but the 244.9Å line, in particular, was so badly affected that it was necessary to exclude the 244.9Å/312.4Å ratio from the minimization. In figure 14 it can be seen that the 244.9Å intensity is particularly high and this appears to be due to blending with a Ni XVI line at 245.7Å. Consequently, the derived value of T_e during this period is expected to be less reliable. At other times the minimization used all six lines.

During much of the NBI phase of the discharge there are small grassy ELMs seen in the D_α

trace in figure 14. The overall shape of T_e(C IV) during this period is similar to the ECE measurement of T_e close to the plasma boundary, although the latter falls after the NBI is switched off at 10s whereas there is a further peak in T_e(C IV). A clear rise in Te(C IV) is seen after the onset of the ITB. There are a number of swings in T_e(C IV), interestingly those during the H-mode period being smaller than in the L-mode phases. This is consistent with the wider temperature range of the L-mode database than the H-mode database illustrated in figures 8 to 10. Although the discursions in T_e(C IV) during the period of 4.5 to 6.3s may be unreliable, a number of the other changes in T_e(C IV) do match particular events in the discharge, this giving confidence that the variations are more than just random noise in the measurement. For example, T_e(C IV) has minima at 4.2s, 8.7s, 9.3s and 11.3s. The first time corresponds to the peak of the first D and H gas puff, the second to the first Ar / Ne emission peak, the third lies between the second Ar / Ne emission peak and the overlapping second D and H gas puff, the last to the third D and H gas puff. A sharp rise in T_e follows the NBI step down at 10.0s and so on. Although the number of events in this pulse leads to possible confusion over the precise interpretation, it does illustrate the possibilities that these data offer for detailed analyses of such events.

Figure 16 shows the D charge exchange contributions to the 312.4Å and 384.1Å lines. It can be seen that the charge exchange contribution to the 312.4Å line is maintained at ~20% after the start of the ITB, whereas that to the 384.1Å line falls with increasing T_e(C IV) as might be expected from figure 7.

CONCLUSIONS

Measurements of the electron temperature of the plasma region that emits C IV radiation from within the JET divertor are presented for a database of Ohmic, L-mode and H-mode phases. Examples of its time development are shown for two Pulse No's: 69937 and 69957. It is found that the C IV temperature range for H-mode discharges (27 to 42eV) is much more limited than for the Ohmic (17 to 48eV) and L-mode phases (23 to 65eV). These ranges are consistent with the values that would be expected from the C IV ion abundance. Under ionization equilibrium, the maximum ion abundance is at an electron temperature of ~7.5eV. Transport of the impurity ions is expected to move the ions to higher temperatures, typically, values of up to the order of the ionization potential, 64.5eV, being reached. The measured temperatures fall within this range. Clear dependences of the C IV temperature on the bulk plasma density are observed for the Ohmic and L-mode phases, for which trends with the bulk plasma T_e are also evident. The D charge exchange recombination contributions to the 312.4Å and 384.1Å lines are found to be significant, varying between 11 to 21% and 0.5 to 4%, respectively. The analysis was not sensitive to dielectronic or radiative recombination for the database used and their contributions must be considered small.

In Pulse No: 69937 the T_e of the divertor C IV emitting plasma is seen to increase at the time of the giant ELMs and in Pulse No: 69957 at the onset of an internal transport barrier, whereas gas puffing tends to decrease the C IV temperature. The accuracy of the T_e measurement is assessed to

be ~±20%, although there are some indications (e.g. figure 15) that its relative accuracy may be better than this. An absolute accuracy of ~±20% is only possible with the availability of new R-matrix calculations of the electron excitation collision strengths and rates covering a wide energy and hence temperature range, combined with an exceptionally accurate sensitivity calibration for the spectrometer used for the observations of the C IV spectrum. The corresponding N V spectrum can also be observed by this spectrometer and a similar analysis is being made for N-seeded discharges. Such analyses provide data that are of value in impurity divertor / edge transport modelling.

The C IV analysis is particularly important in that it shows consistency between the measured line intensity ratios and those derived from the collisional-radiative model to within the order of the experimental accuracy. This means that there is a satisfactory description for the impurity line intensities emitted from the JET divertor. By contrast, significant discrepancies can be observed for measurements made for the SOL using the same instrument and analysis procedure. For example, in an Ohmic database recorded with the spectrometer viewing the SOL just above the throat of the outer divertor, the measured 419.6Å/312.4Å line ratio lies between 0.2 and 0.75 of the ratio expected from the same collisional-radiative model and the 384.1Å/312.4Å ratio can be as low as 0.45 of the expected value. Further work is progressing to gain understanding of these discrepancies.

ACKNOWLEDGEMENTS

This work was carried out within the framework of the European Fusion Development Agreement and was partly funded by the United Kingdom Engineering and Physical Sciences Research Council under grant EP/G003955 and the European Communities under the contract of Association between EURATOM and CCFE. FPK is grateful to AWE Aldermaston for the award of a William Penney Fellowship, while KMA acknowledges financial support form EPSRC. The views and opinions expressed herein do not necessarily reflect those of the European Commission.

REFERENCES

[1]. Aggarwal K.M. and Keenan F.P, 2004, Phys. Scr., **69**, 385

[2]. Burgess A, 1964, 'Proc. of the Symposium on Atomic Collision Processes in Plasmas', Culham Laboratory, AERE - R 4818, 63

[3]. Burke V.M, 1992, J. Phys. B, **25**, 4917

[4]. Fonck R.J, Ramsey A T, Yelle R V, 1982, Appl. Opt., **21**, 2115

[5]. Lawson K.D. *et al*., 2009a, JINST **4** P04013

[6]. Lawson K.D. *et al*., 2009b, JET Report, 'A relative sensitivity calibration of the JET KT7/2 spectrometer'

[7]. Maggi C.F, 1996, Ph.D. Thesis, University of Strathclyde

[8]. Sampson D.H, Zhang H.L, Fontes C.J, 1990, *ADNDT*, **44**, 209

[9]. Schwob J.L, Wouters A.W, Suckewer S, Finkenthal M, 1987, Rev. Sci. Instrum., **58**, 1601

[10]. Summers H.P, 2004, 'The ADAS User Manual, version 2.6, http://adas.phys.strath.ac.uk'
[11]. Whiteford A.D, Badnell N.R, Balance C.P, Loch S.D, O'Mullane M.G, Summers H.P, 2002, *J. Phys. B*, **35**, 3729
[12]. Wolf R.C. *et al*., 1995, JET Preprint, JET-P(95)34
[13]. Zhang H.L, Sampson D H, Fontes C J, 1990, *ADNDT*, **44**, 31

Wavelength (Å)	Transition	Integration range	Blends
244.9	$1s^2 2s\ ^2S_{1/2} - 1s^2 4p\ ^2P_{1/2,3/2}$	±2	
289.2	$1s^2 2p\ ^2P_{1/2,3/2} - 1s^2 4d\ ^2D_{3/2,5/2}$	±2	
296.9	$1s^2 2p\ ^2P_{1/2,3/2} - 1s^2 4s\ ^2S_{1/2}$	±2	
312.4	$1s^2 2s\ ^2S_{1/2} - 1s^2 3p\ ^2P_{1/2,3/2}$	±3	
384.1	$1s^2 2p\ ^2P_{1/2,3/2} - 1s^2 3d\ ^2D_{3/2,5/2}$	±3	CIII, 386.2
419.6	$1s^2 2p\ ^2P_{1/2,3/2} - 1s^2 3s\ ^2S_{1/2}$	±3	

Table 1: C IV lines used in analysis.

	T_e (eV)	n_e (m^{-3})	n_{g+1}/n_g	$n_D n_{g+1}/n_e n_g$
Minimum	10	10^{16}	0.001	0.0001
Maximum	130	10^{21}	10.0	0.05

Table 2: The range of variables used in the 'Constrained_Min' routine.

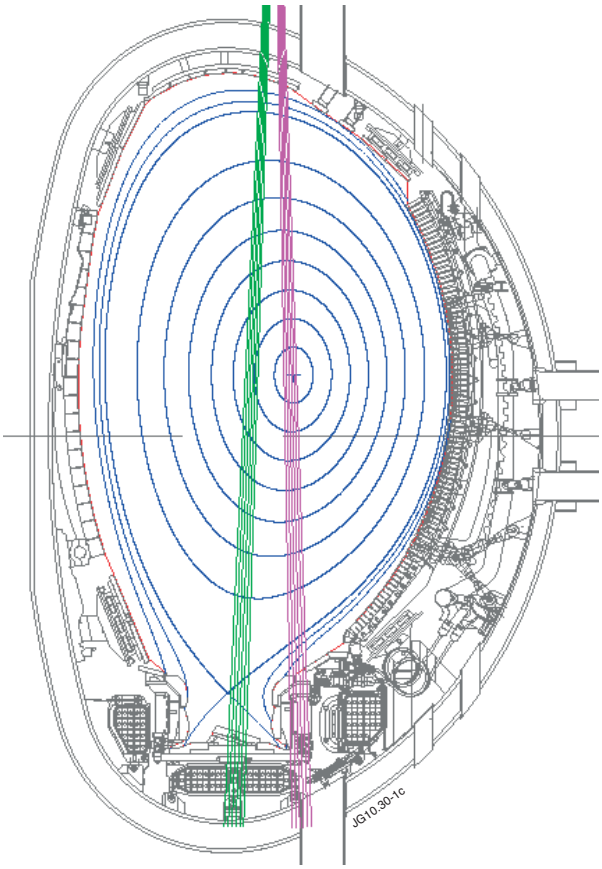

Figure 1: Lines of sight of the JET divertor viewing spectrometer. — divertor view, — view to tiles above outer divertor throat and — magnetic configuration of Pulse No: 69957 at 10s.

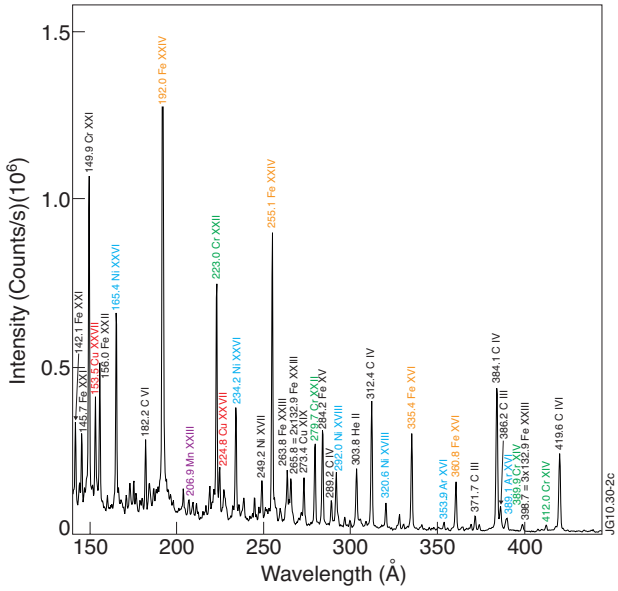

Figure 2: The higher resolution SPRED spectrum for JET Pulse No: 67966 averaged between times 9.3 and 9.4s.

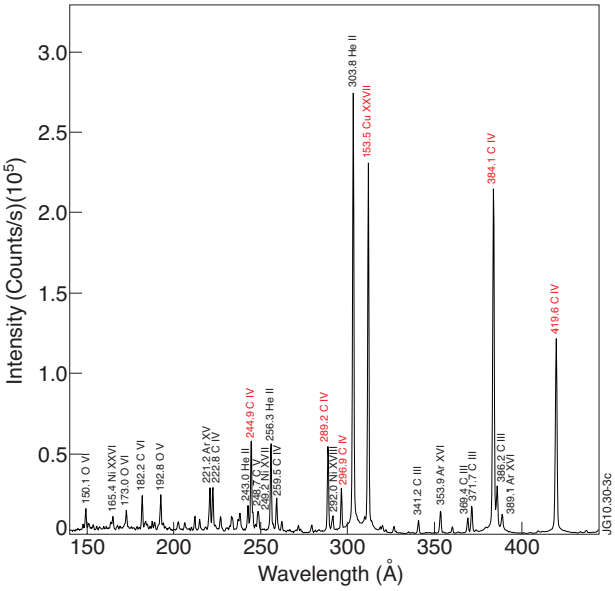

Figure 3: The higher resolution SPRED spectrum for JET Pulse No: 69931 averaged between times 2.3 and 2.6s.

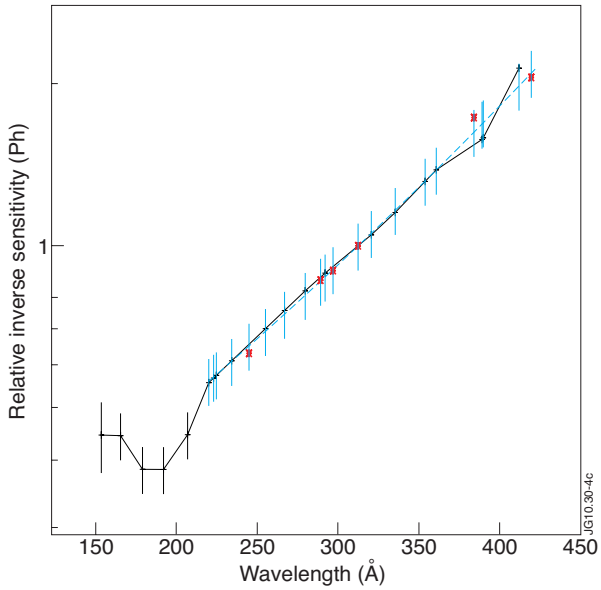

Figure 4: The relative inverse sensitivity calibration (S^{-1} at 312.4Å = 1) for the higher resolution SPRED. + points derived from the Na- and Li-like ratios, ∗ from C IV ratios. – 2nd order polynomial fit.

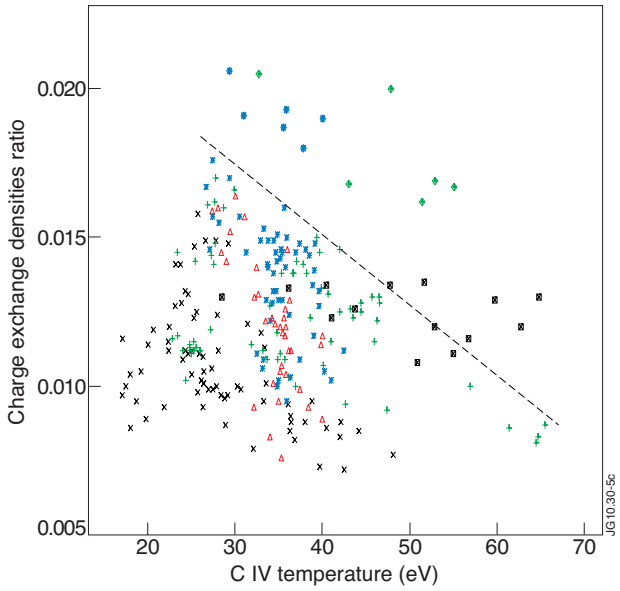

Figure 5: The charge exchange densities ratio, $n_D n_{g+1}/n_e n_g$, plotted against T_e(C IV). × Ohmic, + L-mode, ∗ ELMy H-mode and △ ELM-free H-mode measurements. □ measurements beginning before 2.5s and ◇ affected by N_e impurity gas-puffing.

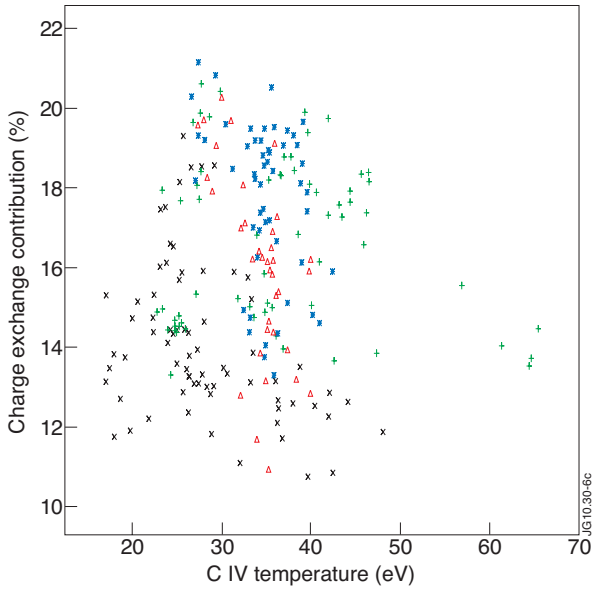

Figure 6: The charge exchange contribution to the 312.4Å line plotted against T_e(C IV). ×Ohmic, + L-mode, ∗ ELMy H-mode and △ ELM-free H-mode measurements.

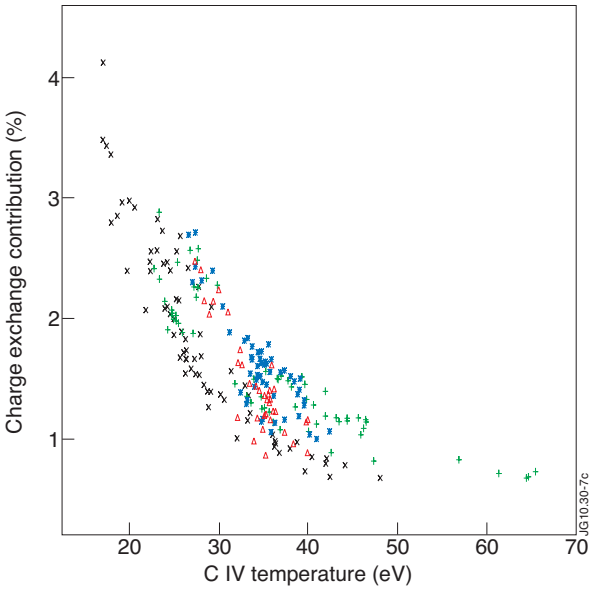

Figure 7: The charge exchange contribution to the 384.1Å line plotted against T_e(C IV). ×Ohmic, + L-mode, ∗ ELMy H-mode and △ ELM-free H-mode measurements.

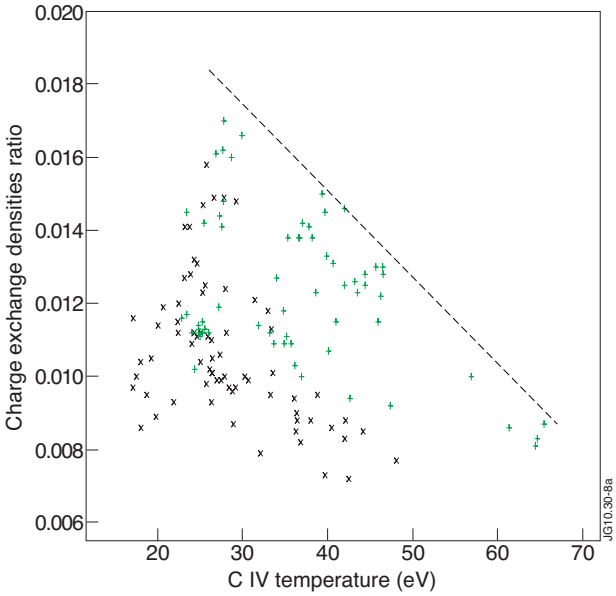

Figure 8a: The charge exchange densities ratio, $n_D n_{g+1}/n_e n_g$, plotted against T_e(C IV). × Ohmic and + L-mode measurements.

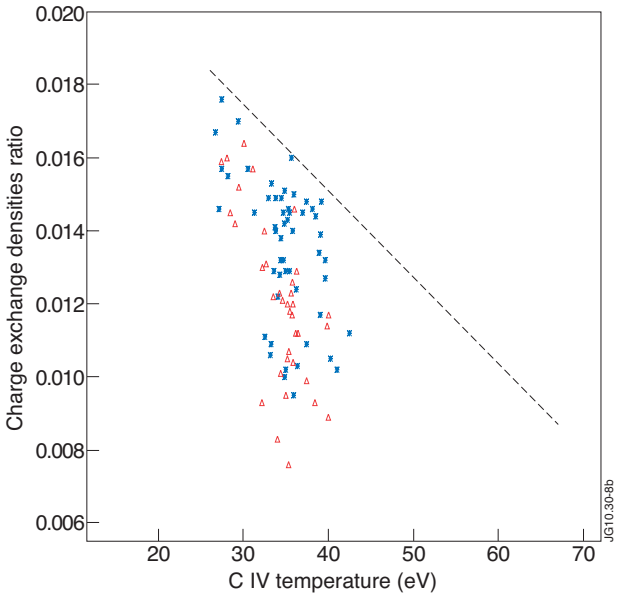

*Figure 8b: The charge exchange densities ratio, $n_D n_{g+1}/n_e n_g$, plotted against T_e(C IV). * ELMy H-mode and △ ELM-free H-mode measurements.*

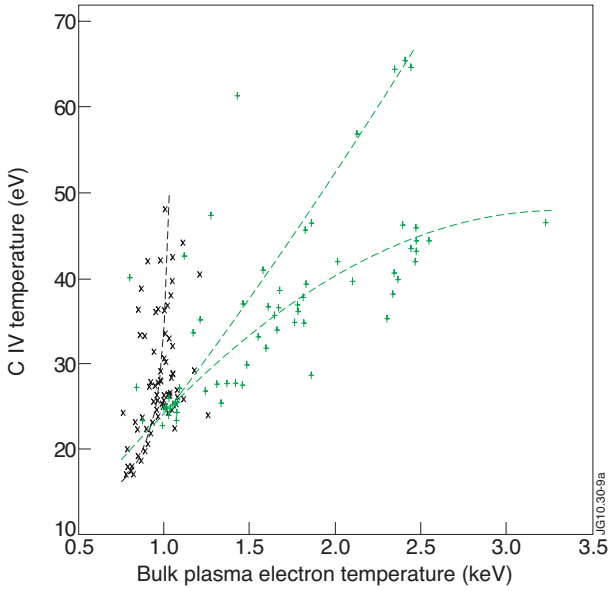

Figure 9a: T_e(C IV) plotted against the bulk plasma T_e. × Ohmic and + L-mode measurements.

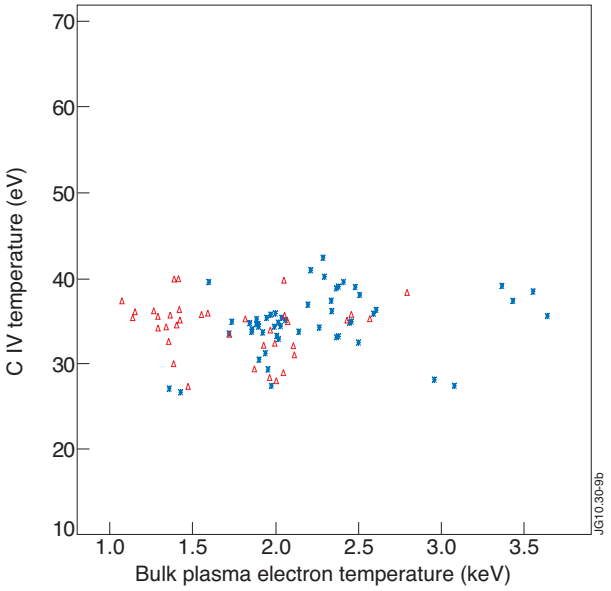

*Figure 9b: T_e(C IV) plotted against the bulk plasma T_e. * ELMy H-mode and △ ELM-free H-mode measurements*

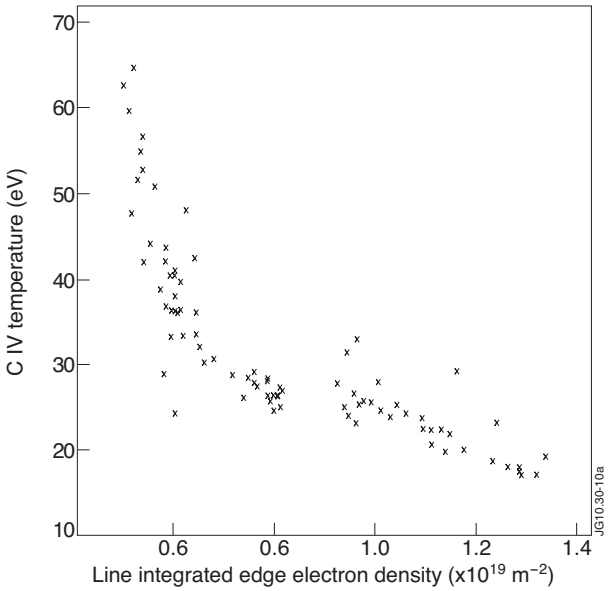

Figure 10a: T_e(C IV) for the Ohmic database plotted against the line integrated edge n_e.

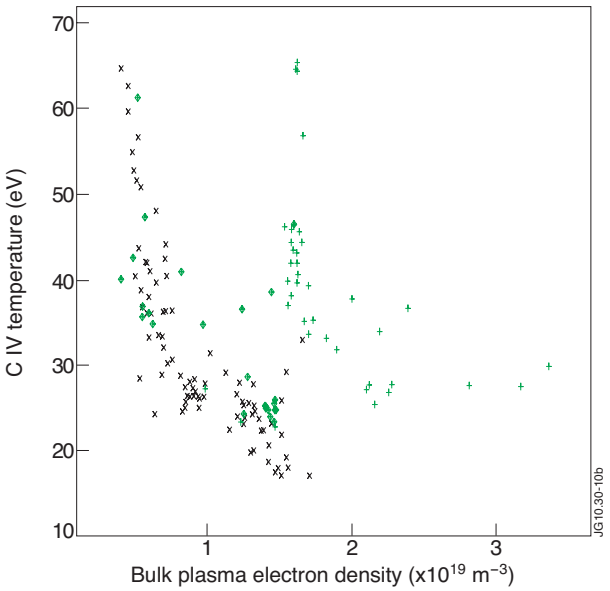

Figure 10b: T_e(C IV) plotted against the bulk plasma n_e. × Ohmic and + L-mode measurements. ◇ L-mode measurements with the outer divertor $D\alpha < 9.0 \times 10^{18}$ ph.s^{-1}.m^{-2}.sr^{-1}.

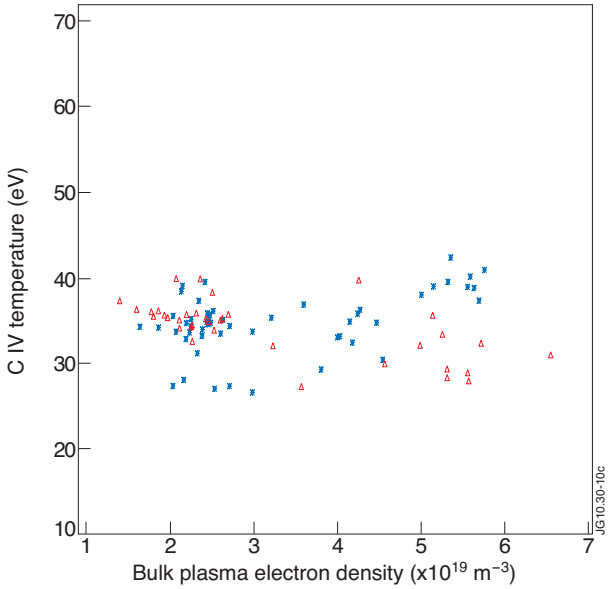

Figure 10c: T_e(C IV) plotted against the bulk plasma n_e. ∗ ELMy H-mode and △ELM-free H-mode measurements.

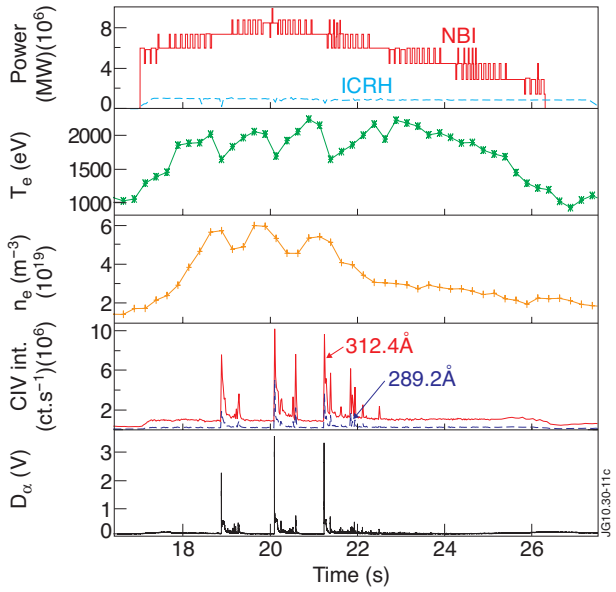

Figure 11: – NBI and – ICRH waveforms, ∗−∗ volume averaged T_e and +−+ volume averaged n_e of the bulk plasma, – 312.4Å and – 289.2Å divertor C IV line intensities and – the D_α measured along an outer vertical line of sight for Pulse No: 69937.

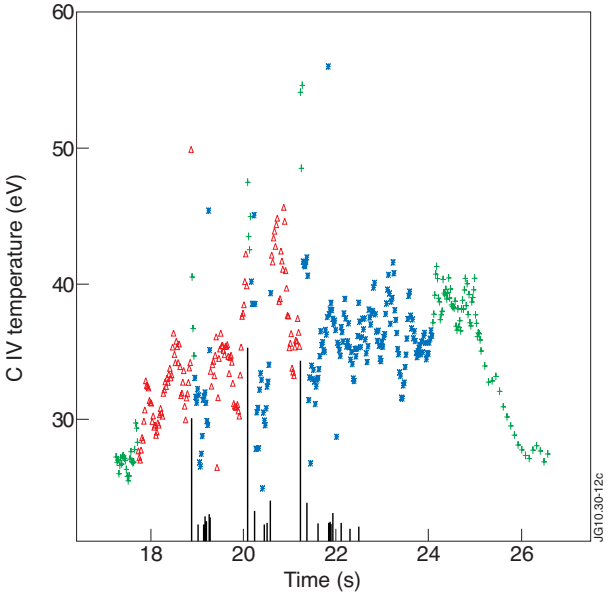

Figure 12: The time development of T_e(C IV) for Pulse No: 69937. + L-mode, ∗ ELMy H-mode and △ ELM-free H-mode measurements. The timing and magnitude of the larger ELMs are indicated by vertical lines.

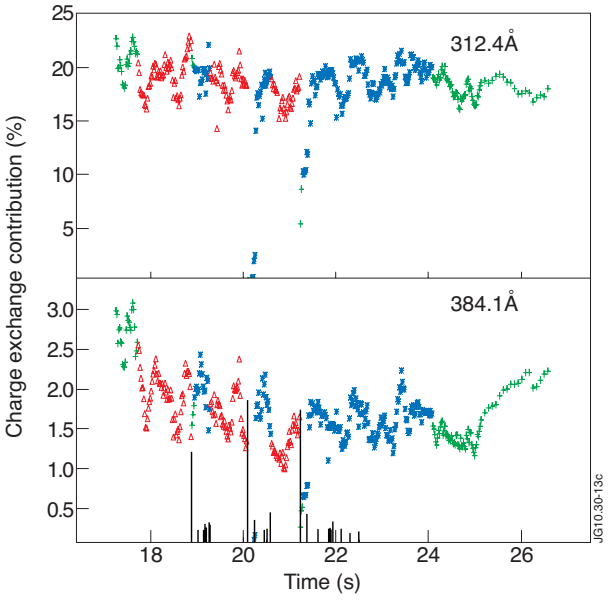

Figure 13: The time development of the charge exchange contributions to the C IV 312.4Å and 384.1Å lines for Pulse No: 69937. + L-mode, ∗ ELMy H-mode and △ ELM-free H-mode measurements. The timing and magnitude of the larger ELMs are indicated by vertical lines.

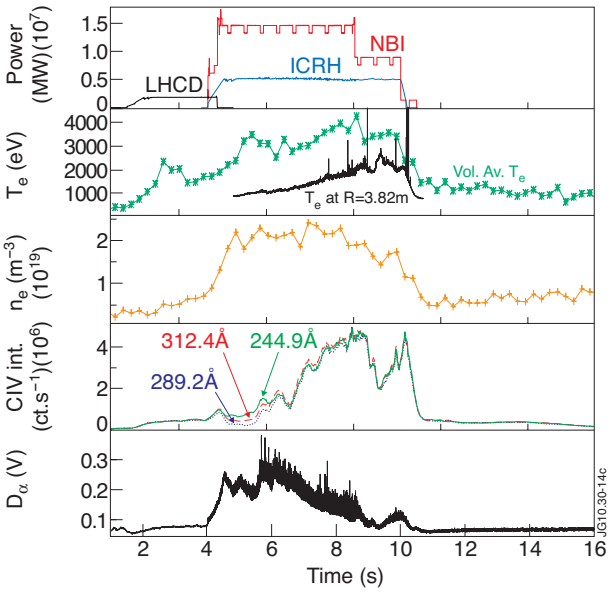

Figure 14: – NBI, – ICRH and – LHCD waveforms, ∗−∗ volume averaged T_e, – T_e measured at a major radius of 3.82m and +−+ volume averaged n_e of the bulk plasma, −− 312.4Å, ···· 4×289.2Å and – 6×244.9Å divertor C IV line intensities and – the D_α measured along an outer vertical line of sight for Pulse No: 69957.

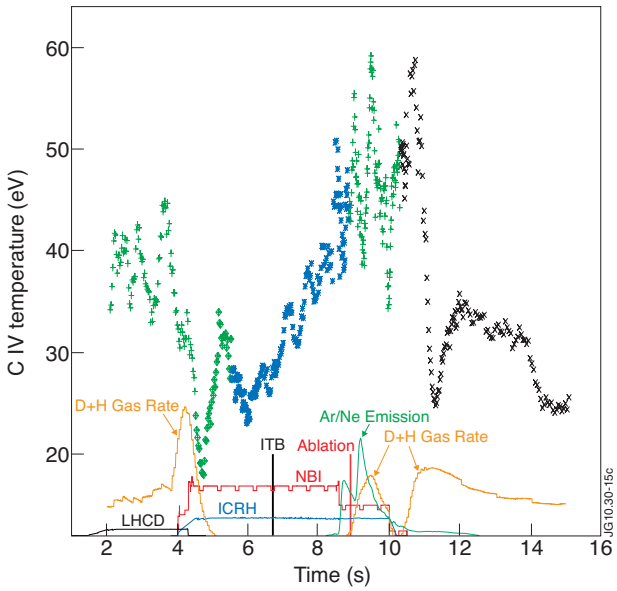

Figure 15: The time development of T_e(C IV) for Pulse No: 69957. × Ohmic, + L-mode and ∗ ELMy H-mode measurements. – NBI, – ICRH and – LHCD waveforms. – D and H gas fuelling rate and – the time development of the Ar/Ne emission. ◇ L-mode and ◇ ELMy H-mode points derived using only a 4 ratio minimization.

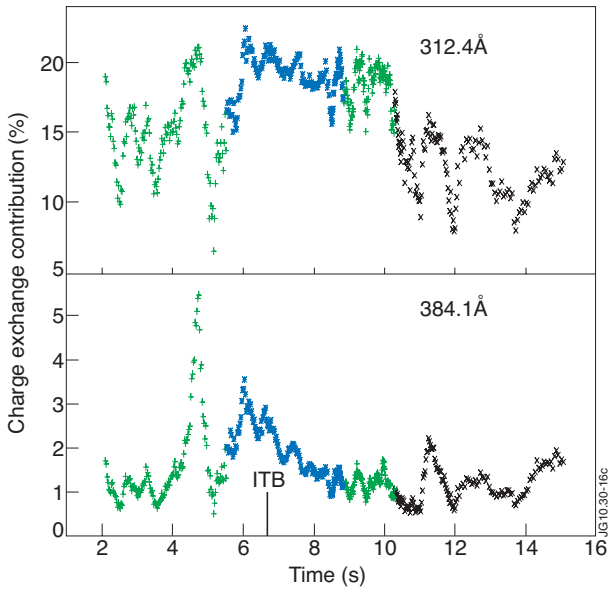

Figure 16: The time development of the charge exchange contributions to the C IV 312.4Å and 384.1Å lines for Pulse No: 69937. × Ohmic, + L-mode and ∗ ELMy H-mode measurements.